The Astrophysical Journal Letters, 911:L17 (7pp), 2021 April 20 https://doi.org/10.3847/2041-8213/abf09b

Keck Cosmic Web Imager Observations of He II Emission in I Zw 18

Ryan J. Rickards Vaught[1], Karin M. Sandstrom[1], and Leslie K. Hunt[2]
[1] Center for Astrophysics and Space Sciences, Department of Physics, University of California, San Diego, 9500 Gilman Dr., La Jolla, CA 92093, USA
rjrickar@ucsd.edu
[2] INAF-Osservatorio Astrofisico di Arcetri, Largo E. Fermi 5, I-50125 Firenze, Italy
Received 2020 October 2; revised 2021 March 8; accepted 2021 March 18; published 2021 April 16

Abstract

With a metallicity of $12 + \mathrm{Log(O/H)} \approx 7.1$–$7.2$, I Zw 18 is a canonical low-metallicity blue compact dwarf (BCD) galaxy. A growing number of BCDs, including I Zw 18, have been found to host strong, narrow-lined, nebular He II (λ4686) emission with enhanced intensities compared to Hβ (e.g., He II(λ4686)/H$\beta > 1\%$). We present new observations of I Zw 18 using the Keck Cosmic Web Imager. These observations reveal two nebular He II emission regions (or He III regions) northwest and southeast of the He III region in the galaxy's main body investigated in previous studies. All regions exhibit He II(λ4686)/Hβ greater than 2%. The two newly resolved He III regions lie along an axis that intercepts the position of I Zw 18's ultraluminous X-ray (ULX) source. We explore whether the ULX could power the two He III regions via shock activity and/or beamed X-ray emission. We find no evidence of shocks from the gas kinematics. If the ULX powers the two regions, the X-ray emission would need to be beamed. Another potential explanation is that a class of early-type nitrogen-rich Wolf–Rayet stars with low winds could power the two He III regions, in which case the alignment with the ULX would be coincidental.

Unified Astronomy Thesaurus concepts: X-ray binary stars (1811); Emission nebulae (461); Blue compact dwarf galaxies (165)

1. Introduction

Narrow-lined, nebular He II(λ4686) emission (He II emission) is observed in an increasing number of blue compact dwarf (BCD) galaxies. Emission from He II arises from the recombination of doubly ionized helium, which requires energetic photons >54 eV. Although there have been several studies into the origin of He II emission (Garnett et al. 1991; Izotov & Thuan 1998; Cerviño et al. 2002; Thuan & Izotov 2005; Kehrig et al. 2011; Shirazi & Brinchmann 2012; Kehrig et al. 2015, 2018; Schaerer et al. 2019; Senchyna et al. 2020) the source(s) of the required ionizing flux remains uncertain.

Of the BCDs that exhibit He II emission, I Zw 18 is of unique interest as it is relatively nearby (18.2 ± 1.5 Mpc; Aloisi et al. 2007), corresponding to a distance modulus of 31.3 Mag, and has one of the lowest metallicities, $12 + \mathrm{Log(O/H)} \approx 7.1$–$7.2$ (R. Vaught et al. 2021, in preparation; Searle & Sargent 1972; Izotov & Thuan 1999; Kehrig et al. 2016, and references therein). He II emission in I Zw 18 has a history of being observed via single-slit spectroscopy (Bergeron 1977; Garnett et al. 1991; Izotov et al. 1997; Izotov & Thuan 1998; Vílchez & Iglesias-Páramo 1998), which has the disadvantage of sparse spatial sampling. Recently, integral field spectroscopy (IFS) of I Zw 18 has spatially resolved the extent of He II emission near the NW stellar cluster (Kehrig et al. 2015).

I Zw 18 also hosts an X-ray binary (XRB), near this He III region. The first reported X-ray luminosity, L_X, of this XRB, via Chandra imaging (Bomans & Weis 2002), was $\sim 10^{39}$ erg s^{-1} in the 0.5–10 keV band (Thuan & Izotov 2005). Kehrig et al. (2015) modeled the XRB contribution to the He II luminosity, $L_{\lambda 4686}$, and found that the predicted $L_{\lambda 4686}$ is $\sim 100\times$ weaker then their observed value. However, deeper XMM-Newton imaging and analysis of the XRB by Kaaret & Feng (2013) report a 0.3–10 keV band luminosity, $L_X = 1.4 \times 10^{40}$ erg s^{-1}, with a harder spectrum than observed with Chandra. With $L_X > 10^{39}$ erg s^{-1} this XRB is considered an ultraluminous X-ray (ULX) source (Pakull et al. 2006; Kaaret & Feng 2013). Although the best fit to the XMM-Newton spectrum, assuming sub-Eddington accretion, suggests a black hole with mass $<154\ M_\odot$ (Kaaret & Feng 2013), recent work suggests that a significant fraction of ULXs are instead stellar-mass binary systems undergoing super-Eddington accretion (King & Lasota 2020, and references therein). Recently, infrared observations and photoionization modeling by Lebouteiller et al. (2017) suggest that I Zw 18's neutral gas heating can be explained by this single XRB, if the 10^4 yr time averaged L_X is 4×10^{40} erg s^{-1}.

In our deeper, higher angular and velocity resolution Keck Cosmic Web Imager (KCWI) observations, we detect two additional He III regions in I Zw 18. These regions are NW and SE of the emission reported by Kehrig et al. (2015), and lie along an axis that intercepts the position of I Zw 18's ULX. The alignment may be coincidental or may suggest that the ULX powers these two regions. We describe our observations and data reduction in Section 2. Our emission line fitting is detailed in Section 2.3. Section 3 outlines how we determine the position of the ULX source. We present our results in Section 4. We discuss possible ionizing sources of the two newly resolved He III regions in Section 5. We conclude this Letter in Section 6.

2. Observations and Data Analysis

2.1. Archival Data

Several archival data sets are used in the course of analyzing our KCWI observations. We downloaded archival Hubble Space Telescope[3] (HST) images in the F439W and F814W

[3] Based on observations made with the NASA/ESA Hubble Space Telescope, and obtained from the Hubble Legacy Archive, which is a collaboration between the Space Telescope Science Institute (STScI/NASA), the Space Telescope European Coordinating Facility (ST-ECF/ESA) and the Canadian Astronomy Data Centre (CADC/NRC/CSA).

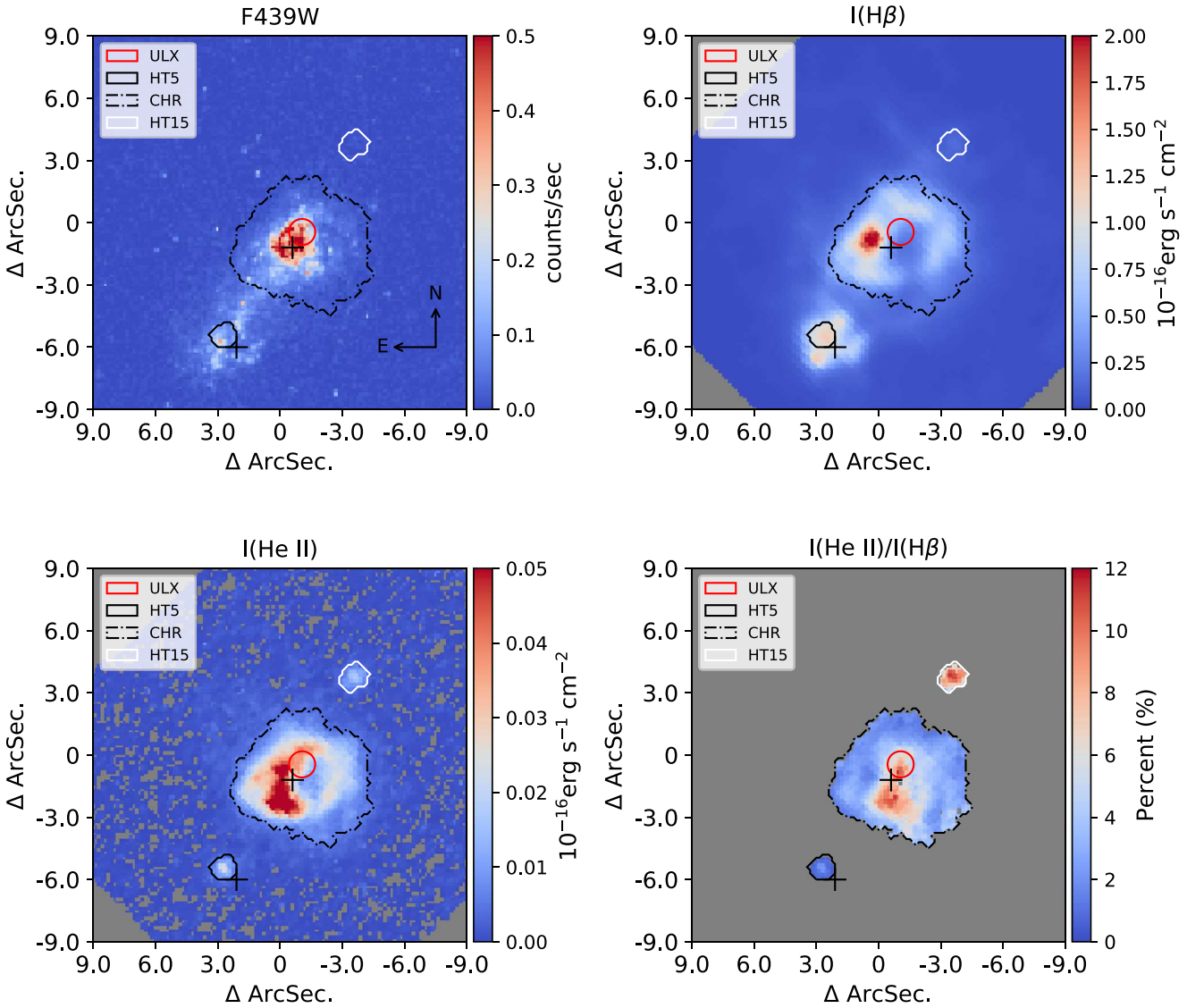

Figure 1. 2D imaging of I Zw 18. Top left: the HST F439W image of I Zw 18 shows the approximate locations of the IZW18-SE/NW (cross-hairs) in comparison to the He III regions. The borders of the three He II emitting regions, HT5 (black dashed), CHR (black solid), and HT15 (white solid) are defined to contain pixels with He II emission S/N > 3. Also shown is the position and astrometric uncertainty of the ULX (red solid). Top right and bottom left: the integrated Hβ and He II emission line maps. Bottom right: He II(λ4686)/Hβ for the three He II emitting regions.

filters (Program IDs: 5434, 10586) as well as *r*-band Sloan Digital Sky Survey (SDSS; Abazajian et al. 2003) images of I Zw 18 (Fields: 157, 158, 238, and 239). To compare with the ULX in I Zw 18, we also downloaded Chandra X-ray imaging of the galaxy (Bomans & Weis 2002).

2.2. KCWI Observations and Data Reduction

The IFS data were taken in clear conditions on 2017 December 25 using KCWI installed on the 10-m Keck II Telescope. We used the small slicer and BL grating centered at 4550 Å with a usable spectral range of 3700-5500 Å. The spectral resolution, $R \sim 3600$ corresponds to an FWHM ~ 1.26 Å at 4550 Å. The slice width is $0\farcs35$. Each pointing covers a field of view (FoV) $8\farcs5$ perpendicular and $20\farcs4$ parallel to the slicer. Using images of the standard star Feige 34, taken in the same conditions, we measured the FWHM of the point-spread function to be $\sim 0\farcs7$.

The main body of I Zw 18 comprises two stellar clusters (IZW18-NW and IZW18-SE; Skillman et al. 1993), shown in Figure 1, and is not covered by a single instrumental FoV. To cover the galaxy, we observed I Zw 18 with four pointings. The exposure per image was 1200 s. To remove the background sky spectrum in each pointing, we integrated for 600 s on an "off" galaxy position between science exposures. We chose the nearest in time sky spectrum to scale and subtract from each science frame. The data were reduced and flux calibrated with the standard star Feige 34 using Version 1.2.1 of the KCWI Data Extraction Reduction Pipeline[4] (Morrissey et al. 2018). The reduced cubes are astrometrically aligned to the HST F814W image, and then placed on a common grid, with pixel size $0\farcs15 \times 0\farcs15$, using the astronomical mosaic image engine `Montage`[5] in combination with custom `Python` scripts. A

[4] https://github.com/Keck-DataReductionPipelines/KcwiDRP
[5] http://montage.ipac.caltech.edu

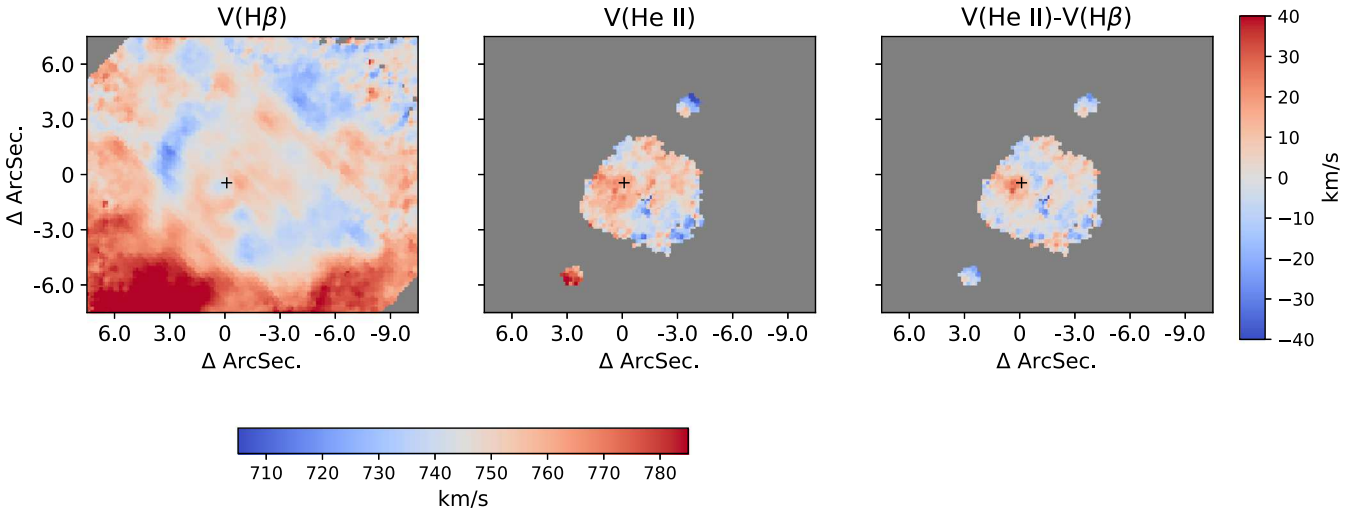

Figure 2. Two-dimensional LZIFU velocity maps. The panels show the velocity maps measured from (left) Hβ, (middle) He II, and (right) the difference between the two velocities. The He II velocities of the HT5 and HT15 regions are very close to the Hβ velocity, traced by Hβ, providing no clear evidence for distinct kinematics in the He II emitting gas. A velocity difference of $\sim$30 km s^{-1} can be seen near the the pixel of peak Hβ emission (+), which has been attributed to a possible supernova remnant (Östlin & Mouhcine 2005).

description of these steps will be presented in R. Vaught et al. (2021, in preparation).

2.3. Emission Line Fitting

Two-dimensional emission line maps were created using LZIFU (Ho et al. 2016). LZIFU simultaneously fits a single (or multi) component Gaussian model to multiple emission lines in a spectrum. The stellar contribution is fit using an implementation of the penalized pixel fitting routine (pPFX; Cappellari & Emsellem 2004). To determine if the observed He II emission line has distinct kinematics, we perform separate LZIFU fits specifically for He II and Hβ alone. These resulting maps are shown in Figures 1 and 2.

3. Astrometry of the ULX Source

To establish how the ULX in I Zw 18 impacts the strength of He II emission it is necessary to determine the location of the ULX. To achieve this, we follow the X-ray source detection procedure in Thuan et al. (2004).[6] Next, we overlay the Chandra source region file on top of *r*-band SDSS images. We chose to match to SDSS imaging rather than HST images because the SDSS imaging covers a larger portion of the Chandra FoV. We are able to determine the positional offsets between the optical/X-ray positions using five X-Ray sources matched to SDSS optical counterparts with rms scatter of $\sim$0.″5. Because the astrometry of our KCWI data is anchored to the F814W HST image, we then compute offsets using a multitude of bright sources in both our SDSS and F814W images. The resulting rms scatter of the offsets is $\sim$0.″2. The position of the ULX in the KCWI image is found after applying the above offsets directly to the Chandra position of the ULX. The final coordinates, ($9^{h}34^{m}1\overset{s}{.}97$, $+55^{d}34^{m}28\overset{s}{.}33$), place the ULX near IZW18-NW, consistent with the position reported in Thuan et al. (2004), with rms scatter 0.″55. The position of the ULX source as it compares to Hβ and He II emission[7] is shown in Figure 1.

4. Results

4.1. 3 He III Regions

Our KCWI observations detect three He III regions. First, northwest of IZW18-NW, and coincident with the H II region HT15 (Hunter et al. 1995) is the He III region that we designate as HT15. Next, coincident with IZW18-SE is a second He III region. This region, whose He II emission has been reported in Skillman et al. (1993) and Izotov et al. (1997), appears to sit close to (or on) the identified H II region HT5 (Hunter et al. 1995); as such we designate this He III region as HT5. The last of the three we define as the central He III region (CHR) as it is coincident with the ionized gas around IZW18-NW and in between HT5 and HT15. CHR corresponds to the region previously mapped in Kehrig et al. (2015). Our observed He II emission map is shown in Figure 1 with the He III regions highlighted.

At a distance of 18.2 Mpc and assuming negligible reddening by dust (for more details on the very low dust attenuation in I Zw 18, see R. Vaught et al. 2021, in preparation; Cannon et al. 2002; Fisher et al. 2014) the total $L_{\lambda 4686}$ measured within the contours, shown in Figure 1, in the CHR is $(102 \pm 15) \times 10^{36}$ erg s^{-1}. $L_{\lambda 4686}$ for the regions HT5 and HT15 are $(1.96 \pm 0.29) \times 10^{36}$ and $(2.05 \pm 0.31) \times 10^{36}$ erg s^{-1}. We also report here the luminosity in Hβ, $L_{\mathrm{H}\beta}$. For CHR $L_{\mathrm{H}\beta}$ is $(288 \pm 43) \times 10^{37}$ erg s^{-1}. $L_{\mathrm{H}\beta}$ for HT5 and HT15 are $(17.7 \pm 2.6) \times 10^{37}$ and $(2.47 \pm 0.37) \times 10^{37}$ erg s^{-1}, respectively. The uncertainties in the reported luminosities are dominated by an estimated calibration error of 15%. HT5 and HT15 are separated by a distance of $\sim$900 pc and are colinear with an axis that runs through the position of the ULX. Because of our high resolution, 0.″7 or $\sim$60 pc at 18.2 Mpc, we are able to resolve the morphology of the He II emitting gas in the CHR of I Zw 18. The He II and Hβ emission trace a horseshoe-like

[6] We run the CIAO, v4.12, wavelet algorithm WAVDETECT on a 0.5–10 keV image, with a probability threshold set to 10^{-7}.

[7] The position of the ULX with that shown in Kehrig et al. (2021) agrees, within positional uncertainties, with this work.

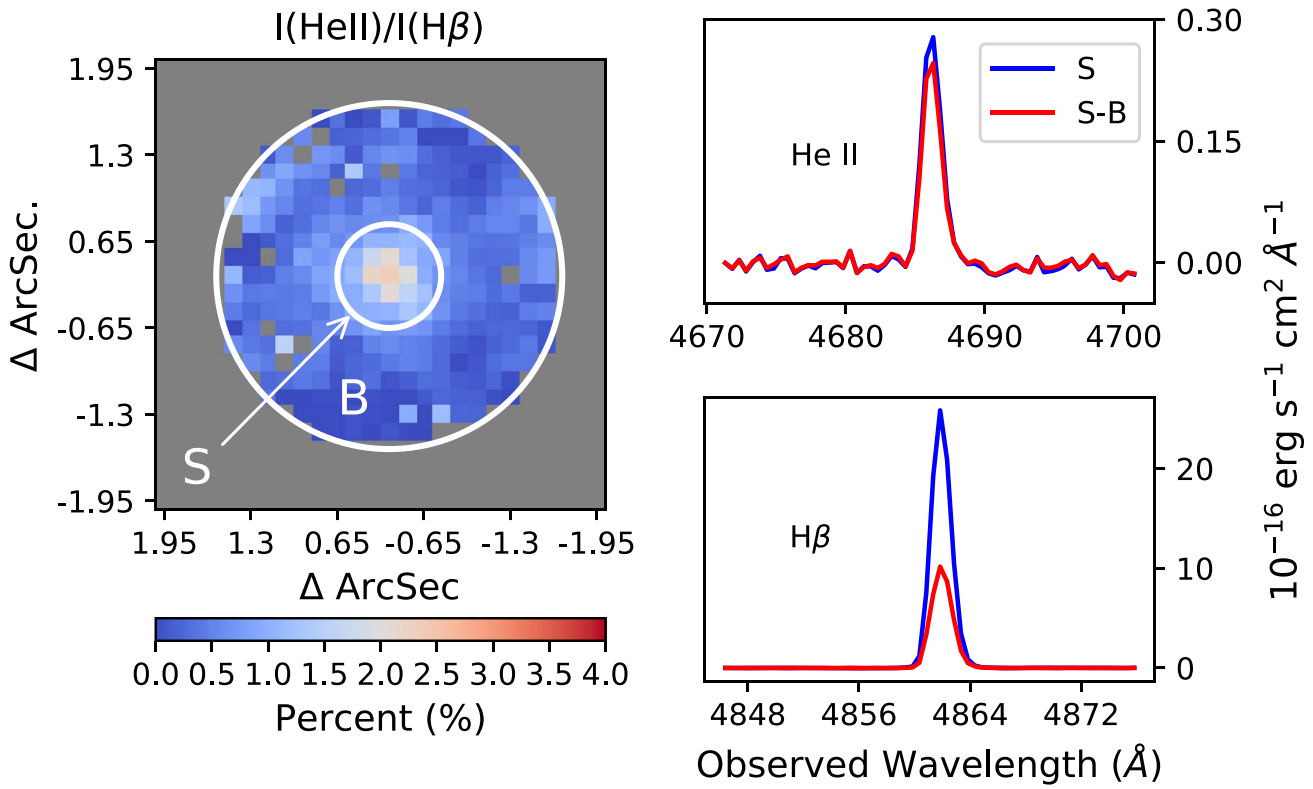

Figure 3. He II(λ4686)/Hβ in HT5. Left: a $4'' \times 4''$ stamp of the 2D map of He II(λ4686)/Hβ in HT5. Contained in the inner annulus is the "source" S and contained in by the outer annulus but outside the inner annulus is the "background" B. Right: the two panels show the continuum-subtracted integrated line profile of He II and Hβ of the source before (blue) and after (red) background subtraction. The "background" contributes a larger fraction to the integrated line intensity of Hβ than to the He II profile.

shell with major/minor diameters of ~550 and 450 pc, respectively. Nearly coincident with the ULX is an apparent cavity, likely created by stellar feedback (Stasińska & Schaerer 1999; Péquignot 2008), with projected radius, $R_C \sim 80$ pc. The He II emission is preferentially extended ~250 pc away from the ULX toward the SE.

To date, there has only been one published IFS analysis of the He II emission in I Zw 18. Kehrig et al. (2015) spatially resolved the He II emission of the CHR and measured a total He II luminosity of $(112 \pm 7) \times 10^{36}$ erg s^{-1}; a factor of 2 less than the value reported in this work. Kehrig et al. (2015) do not report any He II emission near the location of HT5 and HT15. The absence of these regions in their data is expected given their sensitivity.

4.2. The He II(λ4686)/Hβ Ratio

The He II(λ4686)/Hβ intensity ratio is sensitive to shape of the Lyman continuum spectrum shortward of 228 Å, ionization parameter (Garnett et al. 1991; Guseva et al. 2000; Schaerer et al. 2019; Barrow 2020; Stasińska & Schaerer 1999), and/or the shock velocity (Allen et al. 2008). We create a He II (λ4686)/Hβ map by dividing maps of He II and Hβ in regions where signal-to-noise ratio (S/N) > 3 in both lines. This map, shown in Figure 1, reveals He II(λ4686)/Hβ as high as 12% in the CHR and HT15, indicative of a high ionization parameter/harder ionizing spectrum object and/or shocks near the ULX and in HT15. The He II emission along the eastern edge of the shell, and the emission cospatial with the ULX, exhibits the largest He II(λ4686)/Hβ enhancement. Compared to HT15 and the CHR, HT5 exhibits a low peak He II(λ4686)/Hβ value of ~2%. Because HT5 is located within IZW18-SE, there may be excess Hβ emission from gas ionized by stellar sources contributing to the spectrum of HT5. To remove the effects of such an ionized gas component we subtract the median local spectrum in an annulus between 0.″5 and 1″ surrounding HT5. The results of this subtraction are shown in Figure 3; the spectrum of HT5 with the local spectrum removed is revealed to have He II(λ4686)/Hβ closer to ~4.5%.

4.3. Undetected Stellar Continuum in HT15

Of the three regions, HT15 has a nondetected stellar continuum in our observations. This can be seen in Figure 4, where we plot the integrated spectrum of HT15 measured using a ~1 arcsec^2 aperture covering HT15. After adding in quadrature the $\pm 1\sigma$ error spectrum for each pixel, we find that the continuum flux across all wavelengths is within the integrated 1σ errors. If a stellar contribution to the continuum were present, it is undetected below a representative $\bar{\sigma} \approx 1.3 \times 10^{-18}$ erg s^{-1} cm^{-2} Å^{-1}, where $\bar{\sigma}$ is the median 1σ error across all wavelengths. This flux corresponds to a limiting apparent magnitude of $m_V > 24$. This result is similar to those of Hunter et al. (1995) and Hunt et al. (2003), whose Hα and NIR observations of HT15 also lack a measurable stellar component, but instead, only show emission lines from ionized gas. Furthermore, the Hubble Source Catalog (Whitmore et al. 2016) classification of object 766559 at the position of HT15 suggests an extended object, rather than a point source according to photometry in the filters: F450W, F555W, F702W, and F814W.

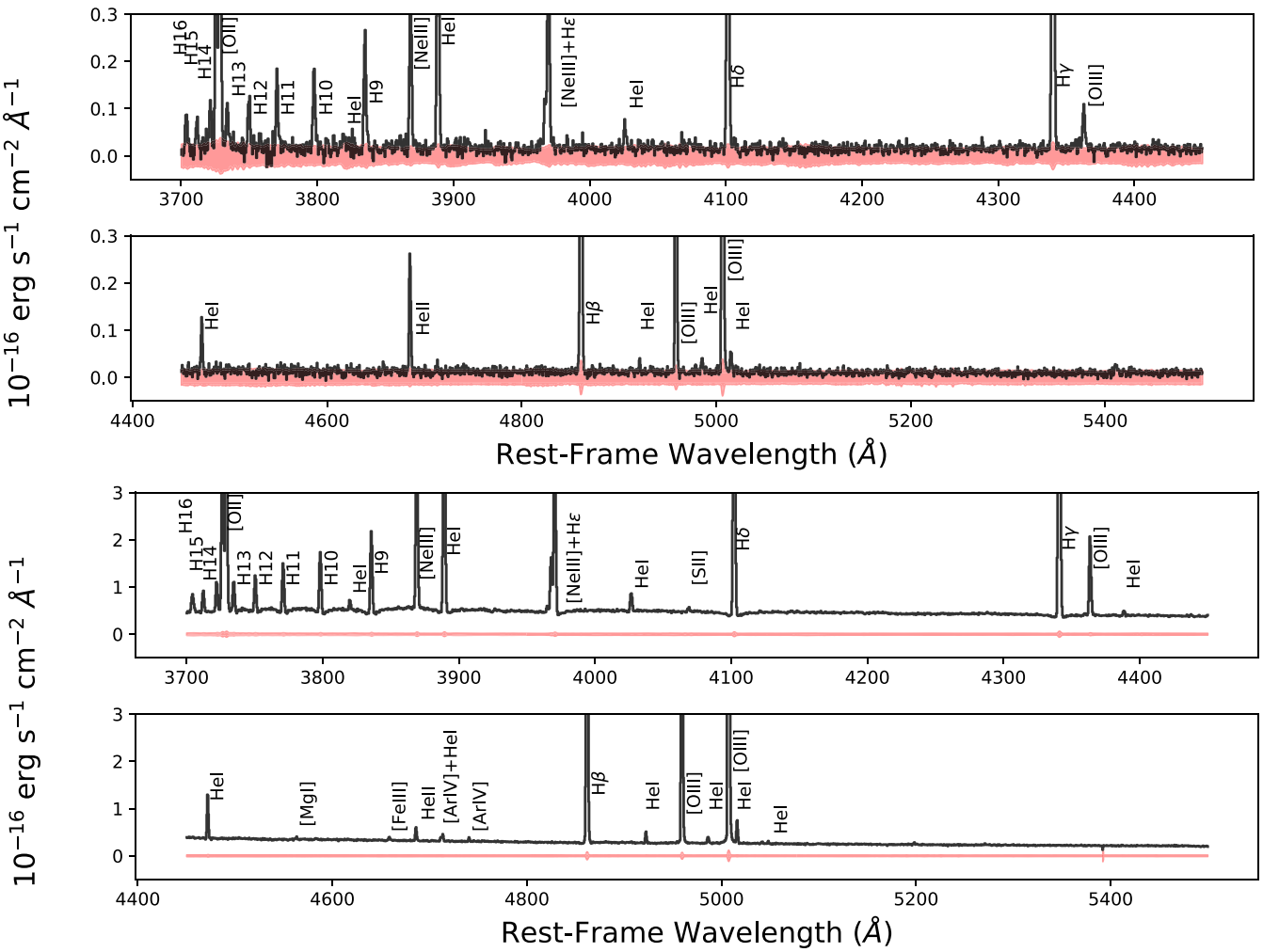

Figure 4. The integrated spectra of HT15 and HT5 (labels of lines shortward/longward of [O II] are shifted 3 Å to the left/right for clarity). Top:t he integrated spectrum of HT15 (black) is shown with the error (red). The continuum flux density of the HT15 region is observed to be within the instrumental noise along the full wavelength range. We infer from this that the HT15 region stellar population is not detected in these data. Bottom: integrated spectrum of HT5. The highest ionization line in either of these spectra is He II(λ4686).

4.4. Kinematics of the He II Gas

To test whether or not the kinematics of He II gas are distinct from that of Hβ, as might be expected if He II emission is the result of shocks while Hβ is largely from photoionization, we perform single line `LZIFU` fits. The results/comparisons of the velocity fits are shown in Figure 2. We find that the difference between the He II and Hβ velocities in the HT15/HT5 regions is negligible, signifying that dynamics of the He II emitting gas around HT15 and HT5 have velocities similar to those traced by Hβ. We measure a velocity difference of $\sim$30 km s^{-1} near the position of peak Hβ emission; however, this may be associated with a supernova remnant or young stellar cluster (Östlin & Mouhcine 2005).

5. Discussion

We use our measurements of the spatial distribution of He II emission in I Zw 18 to discuss possible origins of the high ionization state gas in the two newly resolved He III regions. This includes Wolf–Rayet (WR) stars and ULX-generated phenomena. In the ULX case, the alignment of the two He III regions with the ULX source leads us to explore the possibility that HT15 and HT5 are observable effects from jet/outflow-generated shocks or beamed X-ray emission originating from the ULX. But first, we discuss if Wolf–Rayet stars are consistent with the properties of the He II emission in HT15 and HT5.

5.1. Wolf–Rayet Stars

Although the spectra of HT5 and HT15 lack broad-lined, stellar He II emission, a signature of WR stars (Crowther & Hadfield 2006), we are unable to eliminate these objects as the source of He II emission. The absence of broad-lined, stellar He II emission in our data would be consistent with a population of nitrogen-rich WR (WN) stars, as modeling of WN atmospheres in Crowther & Hadfield (2006) has demonstrated that WN winds are reduced at sub-Large and Small Magellanic Clouds (LMC/SMC) metallicities. Reduced winds diminish the production of broad-lined He II emission, and could explain the absence of this feature in these regions while still potentially powering nebular He II emission.

He III regions have been observed around WN stars Brey2 and AB7 in the LMC and SMC, respectively (Nazé et al. 2003a, 2003b). In Nazé et al. (2003a) the He III region around Brey2 has a He II luminosity, $L_{\lambda 4686} = 3.5 \times 10^{35}$ erg s^{-1}. For

the AB7 He III region, $L_{\lambda4686}$ is 10× greater than Brey2 (Nazé et al. 2003b). Both objects exhibit regions with He II(λ4686)/Hβ greater than 10%. Compared to our HT15 and HT5 $L_{\lambda4686}$ budget, six Brey2-like stars could account for the He II luminosities in HT15 and HT5 while, to order of magnitude, a *single* AB7-like star could solely power He II emission in both HT15 and HT5. Applying the distance modulus to the absolute magnitude, $M_V \sim -3$, for WN stars (Crowther & Hadfield 2006) these populations would not appear brighter than $m_V \sim 24$. WN stars are viable candidates for the production of He II emission in HT15 and HT5.

5.2. Jet or Beamed X-Ray-powered He II Emission in I Zw 18

Supposing that the alignment of HT15 and HT5 with the ULX arises from a physical link, then jet/outflow-generated shocks or beamed X-rays originating from the ULX would be needed to explain the alignment and emission.

Various collisional and radiative processes generated behind shock fronts have been modeled by Allen et al. (2008). This modeling shows that shock speeds between 100 and 150 km s^{-1} can produce He II(λ4686)/Hβ ratios consistent with those observed for HT15 and HT5. Because shock-sensitive lines such as [O I](λ6300), [N II](λ6584), [S II] (λ6717, 6731), and [Ne V](λ3346, 3426) lie outside our spectral range, we are unable to compare to those with shock velocity estimates inferred from He II(λ4686)/Hβ. Kehrig et al. (2016) report measurements of these lines, excluding [Ne V], for the CHR. The observed line ratios are found to be inconsistent with shock ionization. We note that shock templates at I Zw 18-like metallicities are uncertain as shock models only exist for metallicities $\geqslant$SMC. Moreover, the difference between the He II and Hβ derived velocities, as shown in Figure 2, does not show evidence of $\sim$100 km s^{-1} jet/outflow-generated shocks at the locations of HT15 and HT5. The absence of such velocities does not necessarily discount the possibility of jet/outflow activity if the motion were primarily in the plane of the sky. Low spatial resolution radio observations of I Zw 18 by Hunt et al. (2005) show an extended synchotron halo + lobe structure in the radio continuum that they take as evidence of a wind-blown superbubble accompanied by bipolar outflows. However, the direction of these outflows is perpendicular to the axis connecting HT15 and HT5.

Next, we test whether isotropic X-ray emission from the ULX could be sufficient to power the He II emission, or if beaming would be needed. The X-ray flux, using $L_X = 1 \times 10^{40}$ erg s^{-1}, at a distance of, $R \sim 450$ pc, is $F_X \sim 4 \times 10^{33}$ erg s^{-1} pc^2. The power passing through a surface area of πr^2, where r is the radial size of HT15/HT5 with the value $r = 0\farcs3$ or 30 pc, is $P_X = F_X \times \pi r^2 \sim 1 \times 10^{37}$ erg s^{-1}.

As observed in a number of cases and reproduced by photoionization modeling calculations, X-ray ionized nebulae around ULXs appear to exhibit He II emission to total X-ray luminosity ratios of $L_{\lambda4686}/L_X \sim 10^{-4}$ (Pakull & Angebault 1986; Pakull & Mirioni 2002; Kaaret et al. 2004; Kaaret & Corbel 2009; Moon et al. 2011). Assuming this same fraction of power goes into producing He II emission in HT5 and HT15, the power for He II emission is $P_{\lambda4686} = P_X \times 10^{-4} \sim 10^{33}$ erg s^{-1}. When compared to the observed $L_{\lambda4686}$ for HT15/HT5 the He II production budget is short by orders of magnitude. Even using $L_{\lambda4686}/L_X \sim 10^{-2}$, which one gets assuming the ULX is responsible for all of the He II emission in the CHR, the power available to produce He II emission is short by two orders of magnitude. This shows that if the X-ray emission from the ULX powers these two He III regions, the emission needs to be beamed rather than isotropic.

6. Conclusion

We presented KCWI observations of I Zw 18. Our observations revealed the presence of two He III regions, HT15 and HT5, in addition to the He III region mapped by Kehrig et al. (2015). Enhanced He II(λ4686)/Hβ ratios between 4% and up to 12% are measured in HT5 and HT15. Region HT15, which shows some of highest He II(λ4686)/Hβ values, has an undetected stellar population ($m_V > 24$). We compared the observed He II luminosity in HT15 and HT5 to He III regions surrounding LMC/SMC WN stars and find that similar objects are sufficient to produce the He II luminosity and He II(λ4686)/Hβ enhancement of HT15 and HT5 as well as the absence of broad-lined, spectral He II features, while remaining below our detection limit.

Based on the alignment of the two He III regions and the ULX, we explored a scenario in which jet/outflow activity or beamed X-ray emission originating from the ULX powers the observed He II emission in HT15 and HT5. Due to our spectral coverage and the lack of shock models appropriate for the galaxy's metallicity, we cannot put a strong constraint on whether shocks could be powering He II emission. We assessed the velocity structure of the ionized gas and found no kinematic anomalies driven by jet/outflow activity. Assuming that HT15 and HT5 are illuminated by isotropic X-ray emission, we found that the ULX would not produce sufficient X-ray flux to generate the observed He II emission. If the X-ray emission from the ULX powers these sources, it would require beaming. We will present further analysis of the metallicity and temperature structure of I Zw 18 in an upcoming publication.

The authors thank the referee for very thorough and enlightening reports that significantly improved the analysis presented in this Letter. The authors also thank Brent Groves for useful conversations. The data presented herein were obtained at the W. M. Keck Observatory, which is operated as a scientific partnership among the California Institute of Technology, the University of California and the National Aeronautics and Space Administration. The Observatory was made possible by the generous financial support of the W. M. Keck Foundation. The authors wish to recognize and acknowledge the very significant cultural role and reverence that the summit of Maunakea has always had within the indigenous Hawaiian community. We are most fortunate to have the opportunity to conduct observations from this mountain. We also wish to thank Luca Rizzi and all the Keck Observatory staff for observational support. R.R.V. and K.S. acknowledge funding support from National Science Foundation Award No. 1816462. This research made use of Montage. It is funded by the National Science Foundation under grant No. ACI-1440620, and was previously funded by the National Aeronautics and Space Administration's Earth Science Technology Office, Computation Technologies Project, under Cooperative Agreement Number NCC5-626 between NASA and the California Institute of Technology. Funding for the Sloan Digital Sky Survey IV has been provided by the Alfred P. Sloan Foundation, the U.S. Department of Energy Office of Science, and the Participating Institutions.

ORCID iDs

Ryan J. Rickards Vaught https://orcid.org/0000-0001-9719-4080
Karin M. Sandstrom https://orcid.org/0000-0002-4378-8534
Leslie K. Hunt https://orcid.org/0000-0001-9162-2371

References

Abazajian, K., Adelman-McCarthy, J. K., Agüeros, M. A., et al. 2003, AJ, 126, 2081
Allen, M. G., Groves, B. A., Dopita, M. A., Sutherland, R. S., & Kewley, L. J. 2008, ApJS, 178, 20
Aloisi, A., Clementini, G., Tosi, M., et al. 2007, ApJL, 667, L151
Barrow, K. S. S. 2020, MNRAS, 491, 4509
Bergeron, J. 1977, ApJ, 211, 62
Bomans, D. J., & Weis, K. 2002, in ASP Conf. Ser. 262, The High Energy Universe at Sharp Focus: Chandra Science, ed. E. M. Schlegel & S. D. Vrtilek (San Francisco, CA: ASP), 141
Cannon, J. M., Skillman, E. D., Garnett, D. R., & Dufour, R. J. 2002, ApJ, 565, 931
Cappellari, M., & Emsellem, E. 2004, PASP, 116, 138
Cerviño, M., Mas-Hesse, J. M., & Kunth, D. 2002, A&A, 392, 19
Crowther, P. A., & Hadfield, L. J. 2006, A&A, 449, 711
Fisher, D. B., Bolatto, A. D., Herrera-Camus, R., et al. 2014, Natur, 505, 186
Garnett, D. R., Kennicutt, R. C., Jr., Chu, Y.-H., & Skillman, E. D. 1991, ApJ, 373, 458
Guseva, N. G., Izotov, Y. I., & Thuan, T. X. 2000, ApJ, 531, 776
Ho, I. T., Medling, A. M., Groves, B., et al. 2016, Ap&SS, 361, 280
Hunt, L. K., Dyer, K. K., & Thuan, T. X. 2005, A&A, 436, 837
Hunt, L. K., Thuan, T. X., & Izotov, Y. I. 2003, ApJ, 588, 281
Hunter, D. A., Thronson, & Harley, A. J. 1995, ApJ, 452, 238
Izotov, Y. I., Foltz, C. B., Green, R. F., Guseva, N. G., & Thuan, T. X. 1997, ApJL, 487, L37
Izotov, Y. I., & Thuan, T. X. 1998, ApJ, 497, 227
Izotov, Y. I., & Thuan, T. X. 1999, ApJ, 511, 639
Kaaret, P., & Corbel, S. 2009, ApJ, 697, 950
Kaaret, P., & Feng, H. 2013, ApJ, 770, 20
Kaaret, P., Ward, M. J., & Zezas, A. 2004, MNRAS, 351, L83
Kehrig, C., Guerrero, M. A., Vílchez, J. M., & Ramos-Larios, G. 2021, ApJL, 908, L54
Kehrig, C., Oey, M. S., Crowther, P. A., et al. 2011, A&A, 526, A128
Kehrig, C., Vílchez, J. M., Guerrero, M. A., et al. 2018, MNRAS, 480, 1081
Kehrig, C., Vílchez, J. M., Pérez-Montero, E., et al. 2015, ApJL, 801, L28
Kehrig, C., Vílchez, J. M., Pérez-Montero, E., et al. 2016, MNRAS, 459, 2992
King, A., & Lasota, J.-P. 2020, MNRAS, 494, 3611
Lebouteiller, V., Péquignot, D., Cormier, D., et al. 2017, A&A, 602, A45
Moon, D.-S., Harrison, F. A., Cenko, S. B., & Shariff, J. A. 2011, ApJL, 731, L32
Morrissey, P., Matuszewski, M., Martin, D. C., et al. 2018, ApJ, 864, 93
Nazé, Y., Rauw, G., Manfroid, J., Chu, Y. H., & Vreux, J. M. 2003a, A&A, 401, L13
Nazé, Y., Rauw, G., Manfroid, J., Chu, Y. H., & Vreux, J. M. 2003b, A&A, 408, 171
Östlin, G., & Mouhcine, M. 2005, A&A, 433, 797
Pakull, M. W., & Angebault, L. P. 1986, Natur, 322, 511
Pakull, M. W., Grisé, F., & Motch, C. 2006, in IAU Symp. 230, Populations of High Energy Sources in Galaxies, ed. E. J. A. Meurs & G. Fabbiano (Cambridge: Cambridge Univ. Press), 293
Pakull, M. W., & Mirioni, L. 2002, arXiv:astro-ph/0202488
Péquignot, D. 2008, A&A, 478, 371
Schaerer, D., Fragos, T., & Izotov, Y. I. 2019, A&A, 622, L10
Searle, L., & Sargent, W. L. W. 1972, ApJ, 173, 25
Senchyna, P., Stark, D. P., Mirocha, J., et al. 2020, MNRAS, 494, 941
Shirazi, M., & Brinchmann, J. 2012, MNRAS, 421, 1043
Skillman, E. D., & Kennicutt, R. C., Jr. 1993, ApJ, 411, 655
Stasińska, G., & Schaerer, D. 1999, A&A, 351, 72
Thuan, T. X., Bauer, F. E., Papaderos, P., & Izotov, Y. I. 2004, ApJ, 606, 213
Thuan, T. X., & Izotov, Y. I. 2005, ApJS, 161, 240
Vílchez, J. M., & Iglesias-Páramo, J. 1998, ApJ, 508, 248
Whitmore, B. C., Allam, S. S., Budavári, T., et al. 2016, AJ, 151, 134